# Mesh Adaptation for Computational Fluid Dynamics 2

*Unsteady and*
*Goal-oriented Adaptation*

Alain Dervieux
Frédéric Alauzet
Adrien Loseille
Bruno Koobus

Color Section

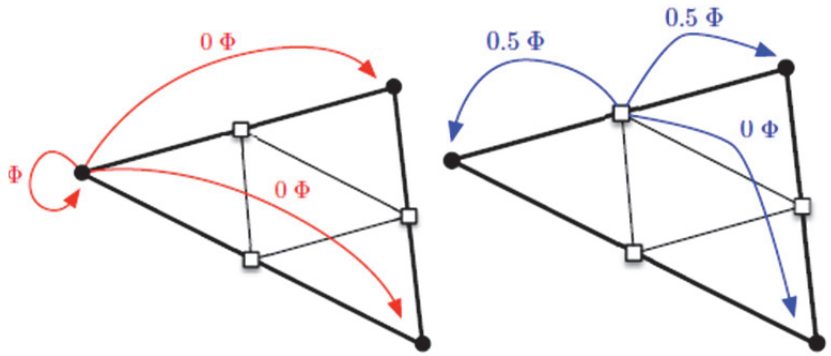


**Figure 1.1.** *Examples of linear accumulation process when the $h/2$-mesh vertex $Q_k$ coincides with the $h$-mesh vertex $P_i$ (left) and when the $h/2$-mesh vertex $Q_k$ is the mid-point of a $h$-mesh edge $e$ (right).*

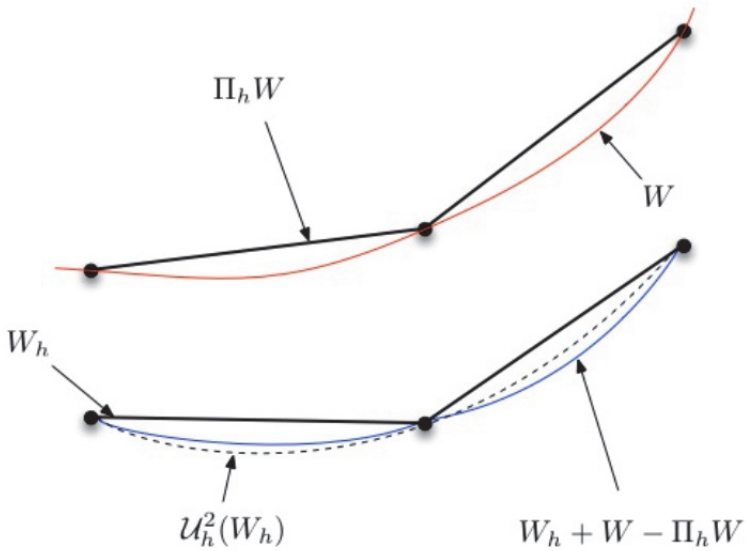


**Figure 1.2.** *Reconstruction of a smoother solution (dashed curve) from a discrete solution (straight segments) compared to the exact solution (W) and the reconstructed solution with the exact defect (Wh +W − ΠhW)*

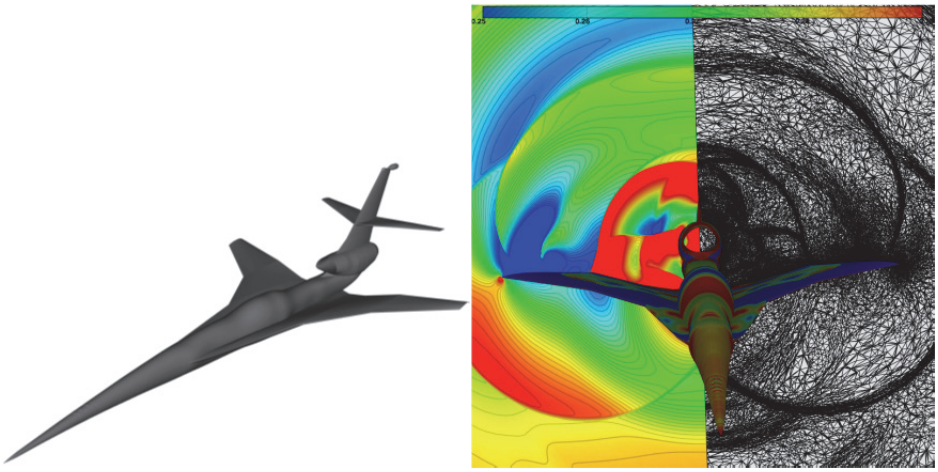

**Figure 1.3.** *Second AIAA Sonic Boom prediction workshop. Left: C25D geometry. Right: Cut plane in the volume behind the aircraft where we can observe in the left part the Mach field and in the right part the 5.9 million vertices adapted mesh obtained with a goal-oriented mesh adaptation on the pressure signature*

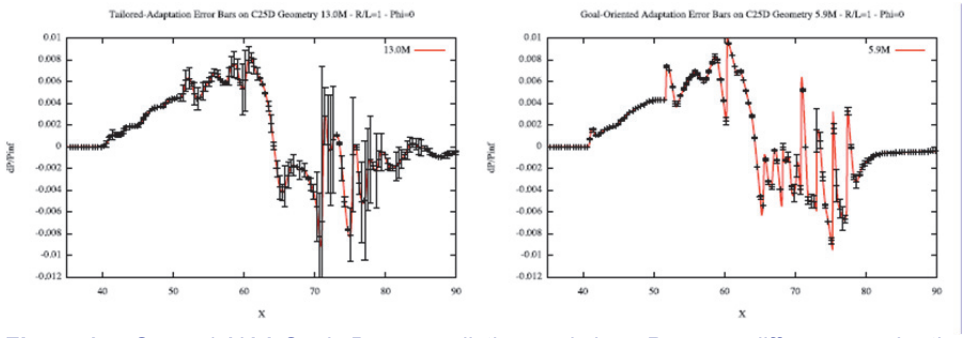


**Figure 1.4.** *Second AIAA Sonic Boom prediction workshop. Pressure difference under the plane (continuous line) for a tailored mesh (left) composed of 13 million vertices and adapted meshes (right) composed of 5.9 million vertices. The estimated error provided by the nonlinear corrector is shown by the vertical error bars*

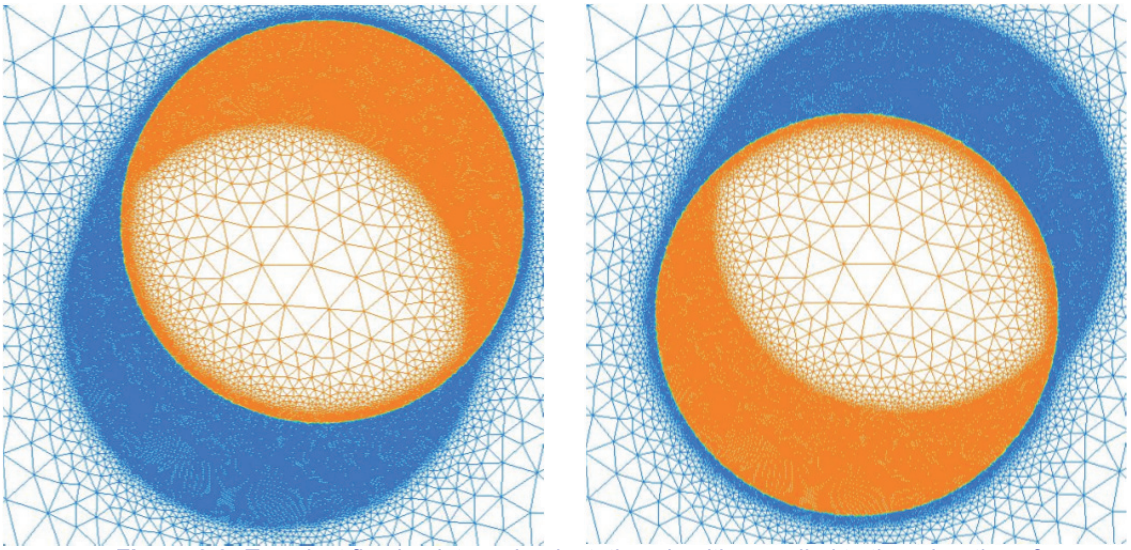

**Figure 2.2.** *Transient fixed-point mesh adaptation algorithm applied to the advection of a circle-shaped discontinuity between a region where physical density is equal to 1 (blue) a region where it is equal to 2 (orange). Left, the interface at time $t_i$. Right, the interface at time $t_{i+1}$. On both pictures, the adapted mesh for advection during the time interval $[t_i, t_{i+1}]$*

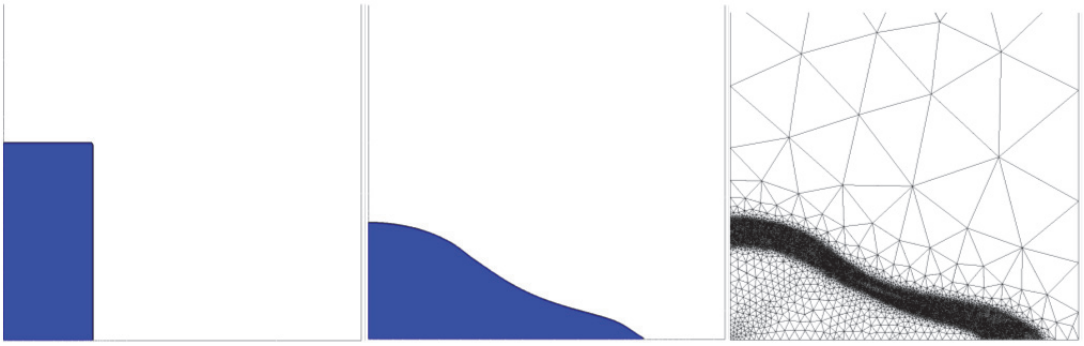

**Figure 2.4.** *2D falling water column. Interfaces at $t = 0$ and $t = 2$ and mesh at $t = 2$*

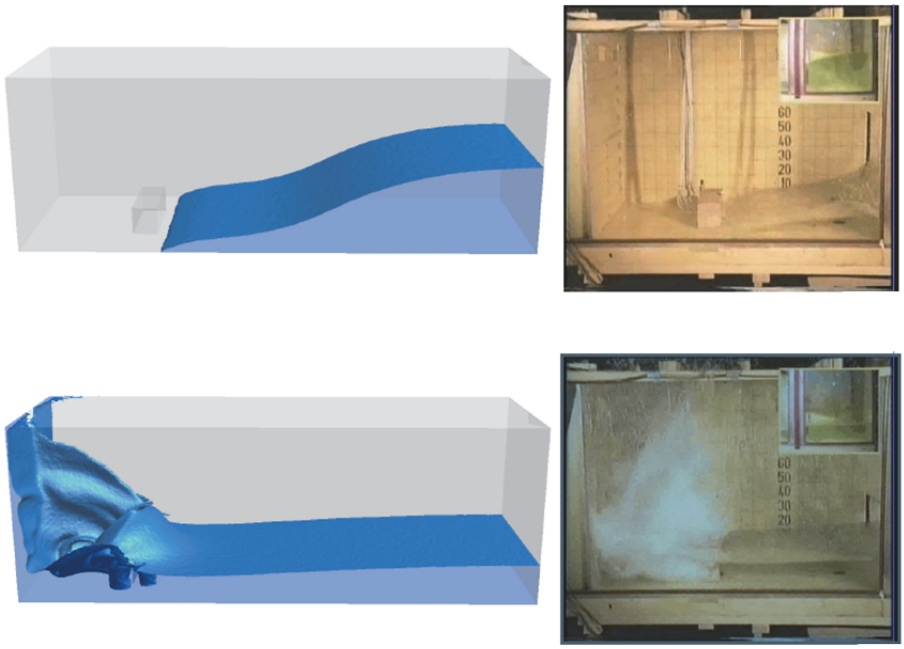

**Figure 2.7.** *3D falling water column on a obstacle. Comparison between the interface obtained in the simulation (left) and the pictures from the MARIN experiment (right). From top to bottom, snapshots for every 0.4 s, for times $t$ = 0.4 s and $t$ = 1.6 s*

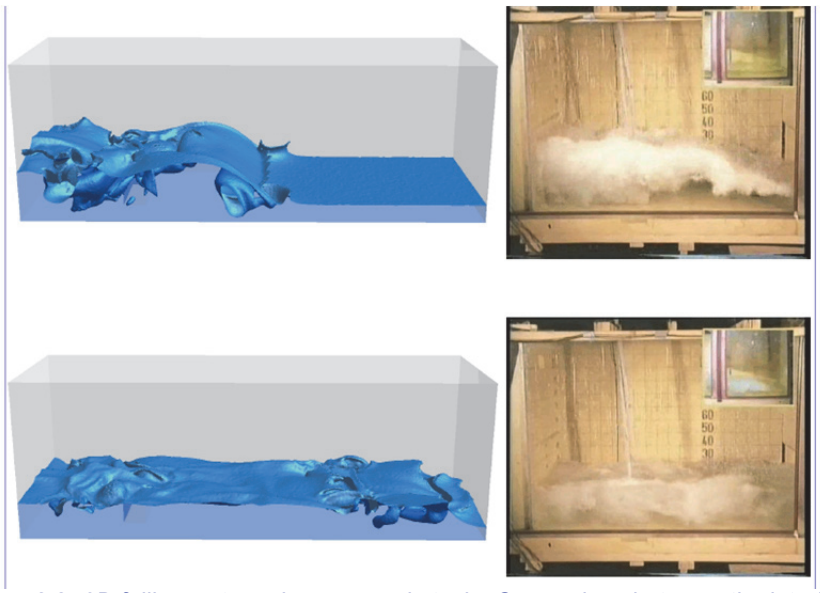

**Figure 2.8.** *3D falling water column on a obstacle. Comparison between the interface obtained in the simulation (left) and the pictures from the MARIN experiment (right). From top to bottom, snapshots for $t$ = 2.4 s and $t$ = 5.6 s*

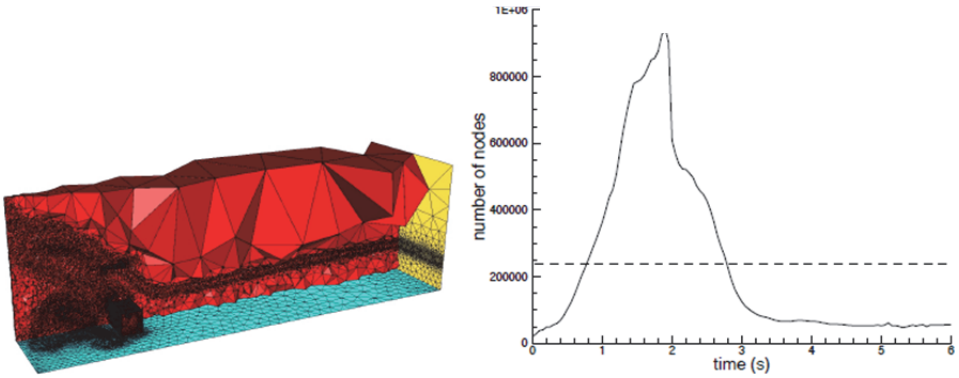


**Figure 2.9.** *3D falling water column on a obstacle. Mesh adaptation based on the interface and moments. Left: An example of mesh used during a time subinterval, around $t$= 1.2s. The mesh involves ≈ 500,000 vertices. Right: Variation of the number of mesh vertices as a function of time. The dashed line represent the average number of vertices for the whole simulation ≈ 240,000 vertices*

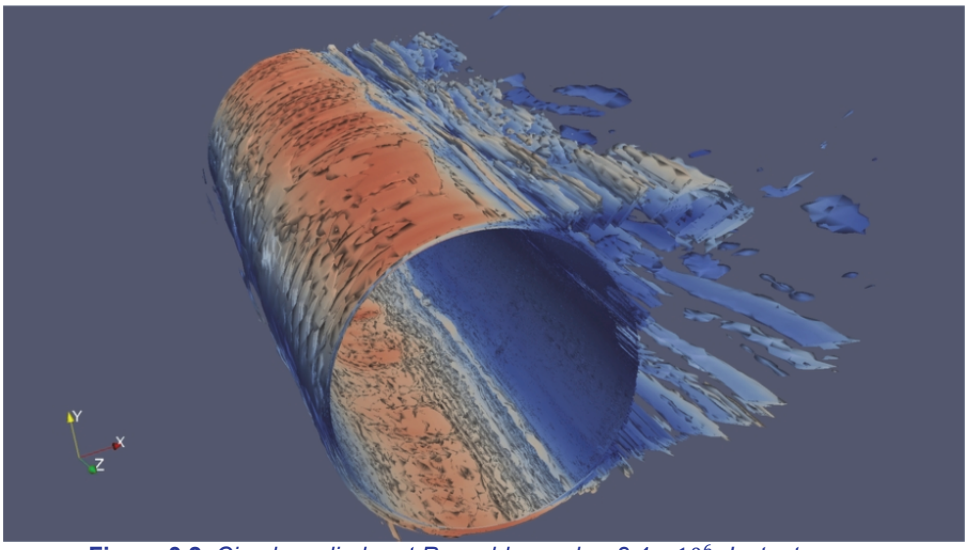


**Figure 3.2.** *Circular cylinder at Reynolds number 8.4 × $10^6$. Instantaneous Q-criterion isosurfaces (colored with velocity modulus)*

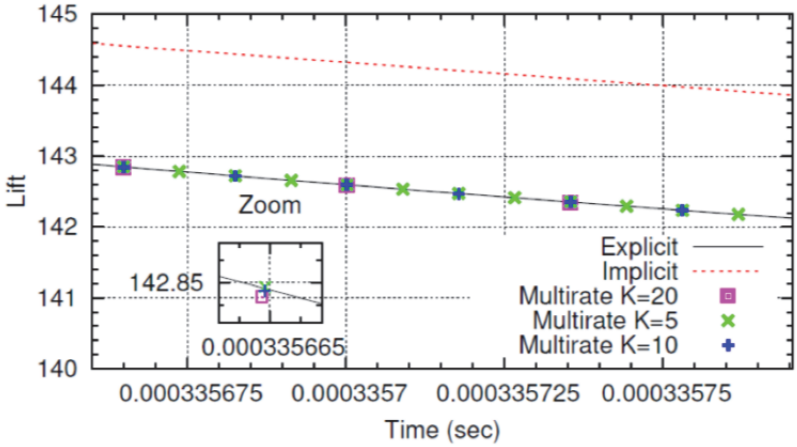


**Figure 3.3.** *Circular cylinder at Reynolds number 8.4× $10^6$. Zoom of the lift curves obtained with explicit, implicit and MR schemes*

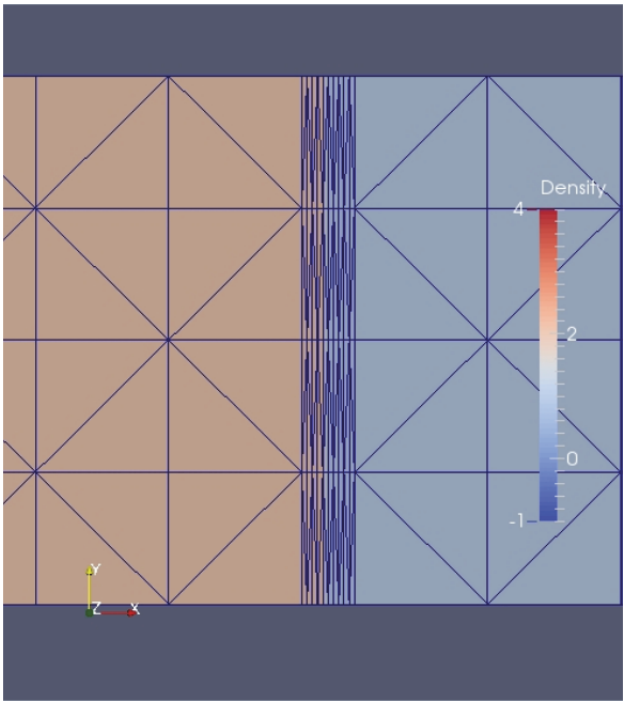


**Figure 3.4.** *Mesh adaptative calculation of a traveling contact discontinuity. Instantaneous mesh with mesh concentration in the middle of zoom and corresponding advected discontinuous fluid density. Density is 3 on the left, 1 on the right*

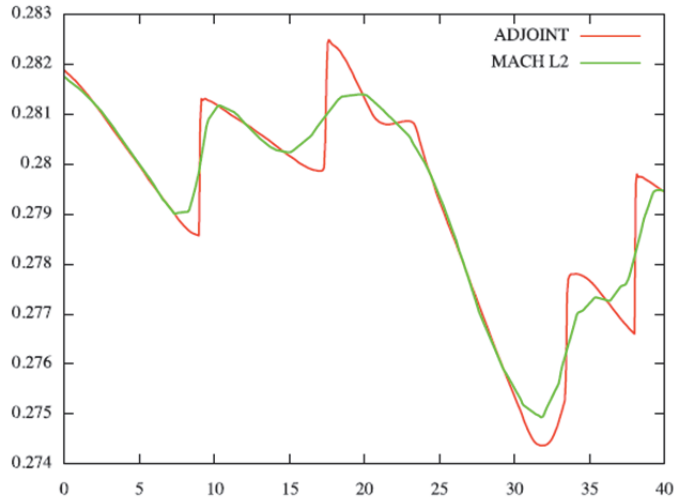


**Figure 4.2.** *Pressure signature along x axis in the observation plane Adjoint based calculation produces very stiff shock capturing (quasi vertical segments)*

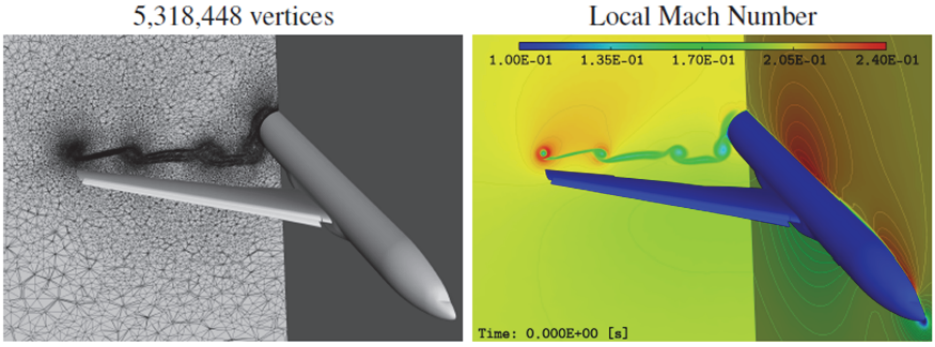


**Figure 5.2.** *HL-CRM* $16^{\circ}$ *case. Cut plane* $x = 50$. *The 5M vertices adapted mesh obtained with the viscous goal-oriented error estimate (left) and the associated local Mach number solution (right)*

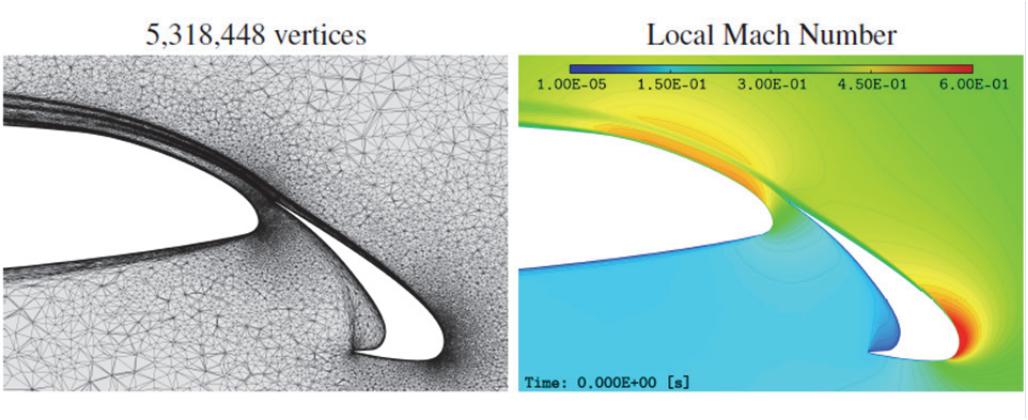


**Figure 5.3.** *HL-CRM* $16^{\circ}$ *case. Cut plane* $y = 15.5$ *(near the flap). The 5M vertices adapted mesh obtained with the viscous goal-oriented error estimate (left) and the associated local Mach number solution (right)*

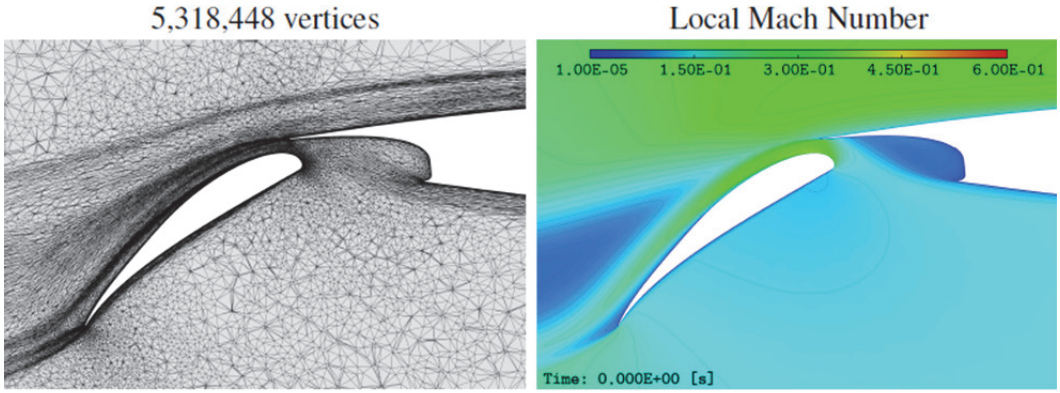


**Figure 5.4.** *HL-CRM* $16^{\circ}$ *case. Cut plane* $y = 15.5$ *(near the slat). The 5M vertices adapted mesh obtained with the viscous goal-oriented error estimate (left) and the associated local Mach number solution (right)*

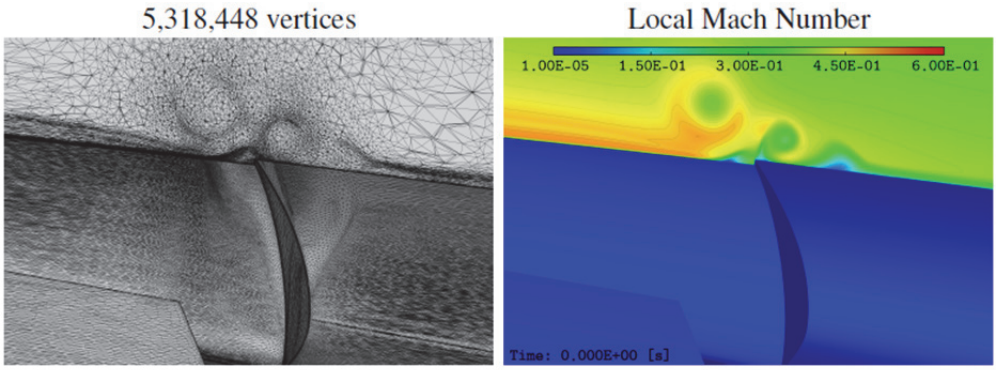


**Figure 5.5.** *HL-CRM* $16^{\circ}$ *case. Cut plane in the region where the slat tip vortex interacts with the main wing. The 5M vertices adapted mesh obtained with the viscous goal-oriented error estimate (left) and the associated local Mach number solution (right)*

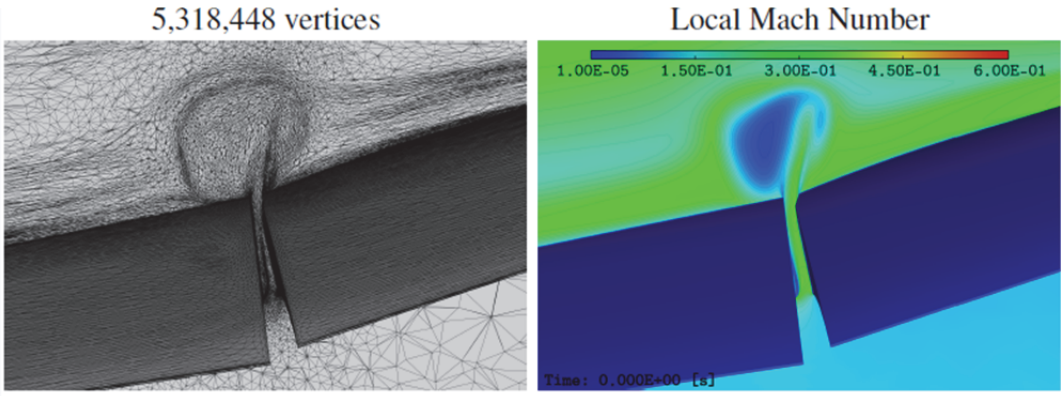


**Figure 5.6.** *HL-CRM* $16^{\circ}$ *case. Cut plane* $x = 38$ *(near the gap between the flaps). The 5M vertices adapted mesh obtained with the viscous goal-oriented error estimate (left) and the associated local Mach number solution (right)*

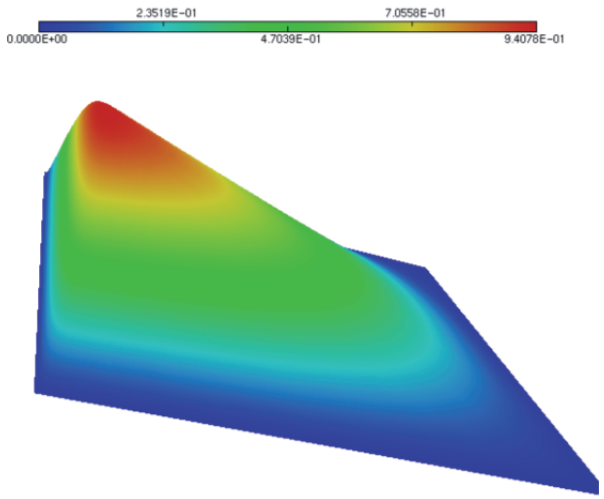


**Figure 6.1.** *Fully 2D boundary layer test case: sketch of the solution*

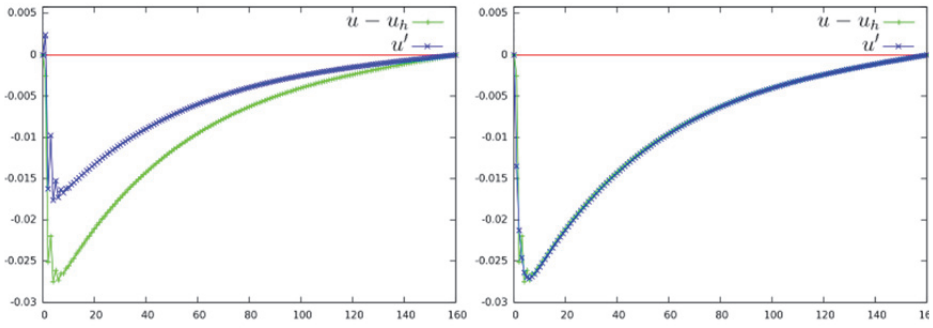


**Figure 6.2.** *Fully 2D boundary layer test case. Left: Comparison of the a priori corrector $u'_{prio}$ $(\times)$ with approximation error $u - u_h$ $(+)$, error cuts for $y = 0.5$. The a priori corrector is able to correct about 60% of the approximation error amplitude. Right: Comparison of the defect-correction corrector $u'_{DC}$ $(\times)$ with the approximation error $(+)$, error cuts for $y = 0.5$. The defect-correction corrector is able to correct about 95% of the amplitude.*

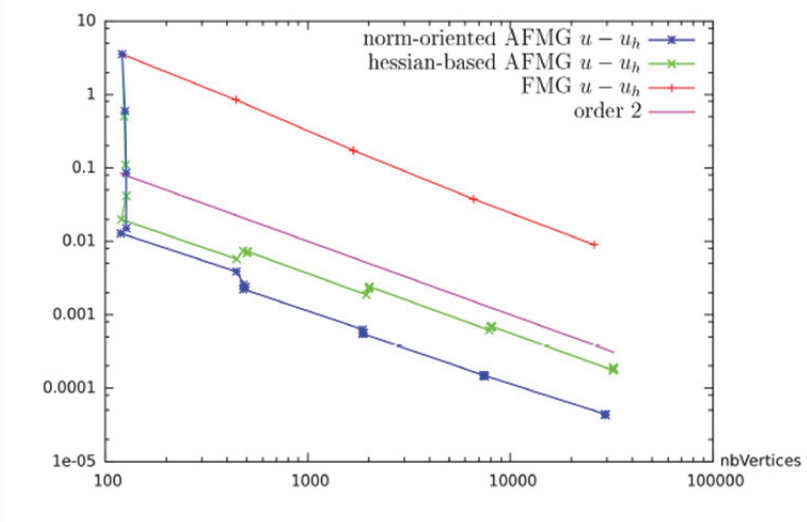


**Figure 6.3.** *Fully 2D boundary layer test case: convergence of the error norm $|u-u_h|_{L^2}$ as a function of number of vertices in the mesh for (+) non-adaptative FMG, (×) Hessian-based adaptative FMG and (∗) norm-oriented adaptative FMG. The quasi-vertical segments at abscissa $nbVertices \approx 128$ corresponds to the error reduction by the anisotropic mesh adaptation at constant complexity (i.e. quasi-constant number of vertices). These quasi-vertical segments corresponding to anisotropic adaptation phases also appear (less clearly) for abscissae $nbVertices \approx 512, 2048, 8196$. Oblique segments correspond to phases in which all the elements of the mesh are purely divided in four subelements by using mid-edges. As can be expected, the mesh division produces a reduction of the error by a factor of four because of second-order convergence. In contrast, anisotropic adaptation produces a tremendous error reduction for 128 vertices and not so much for the higher number of vertices. Our interpretation of this is that the main detail, the boundary layer, involves a single scale, it thickness (no smaller detail exists inside the boundary layer or elsewhere), and once the mesh has taken into account this scale, no important further improvement is possible. A last remark is that the norm-oriented approach delivers a convergence order slightly better than two while the feature-based approach delivers a slightly degraded convergence for the finer mesh, confirming that the best mesh for interpolation is not the best mesh for approximation.*

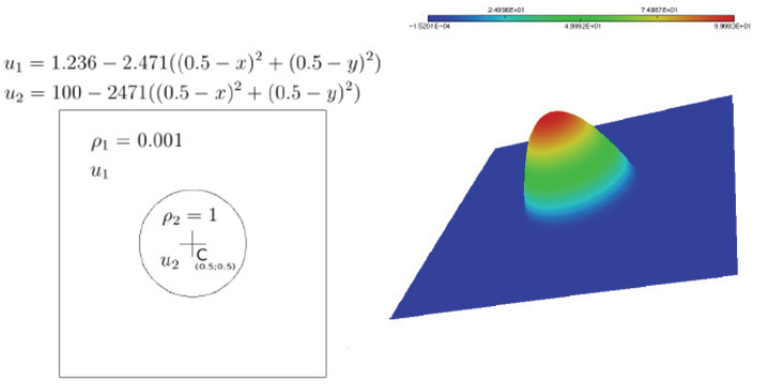


**Figure 6.4.** *Poisson problem with discontinuous coefficient: sketch of exact solution definition and a typical computation of it*

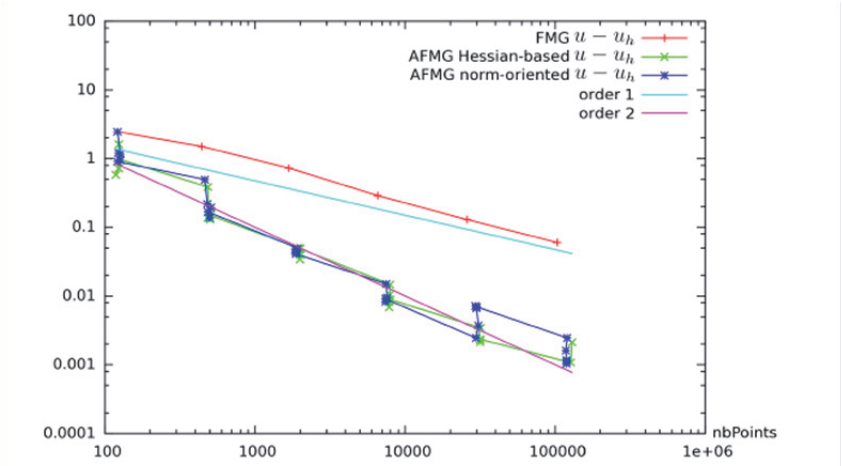


**Figure 6.6.** *Poisson problem with discontinuous coefficient. Convergence of the error norm $|u-u_h|_{L^2}$ as a function of number of vertices in the mesh for nonadaptative FMG (+), Hessian-based adaptative FMG ($\times$) and norm-oriented adaptative FMG ($*$). The non-adaptive convergence is solely a first-order one as expected for a singular solution. The two mesh-adaptation approaches produce second-order accuracy. Note that the mesh adaptation bonus appears in good part during the mesh enrichment phases.*

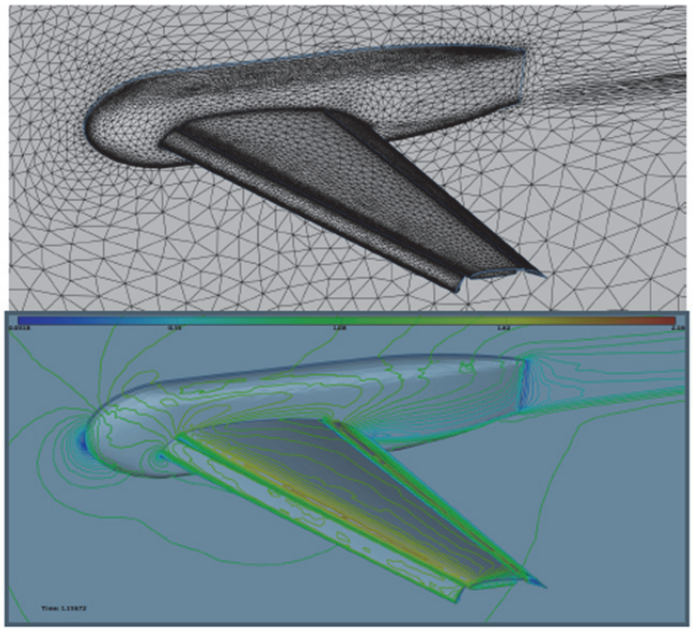

**Figure 6.7.** *Feature-based adaptation for minimizing the $L^1$ norm of the interpolation error on the density, velocity and pressure. Top: View of the skin mesh. There is not much mesh concentration on the body in the wake of wing. Bottom: Velocity on the aircraft skin*

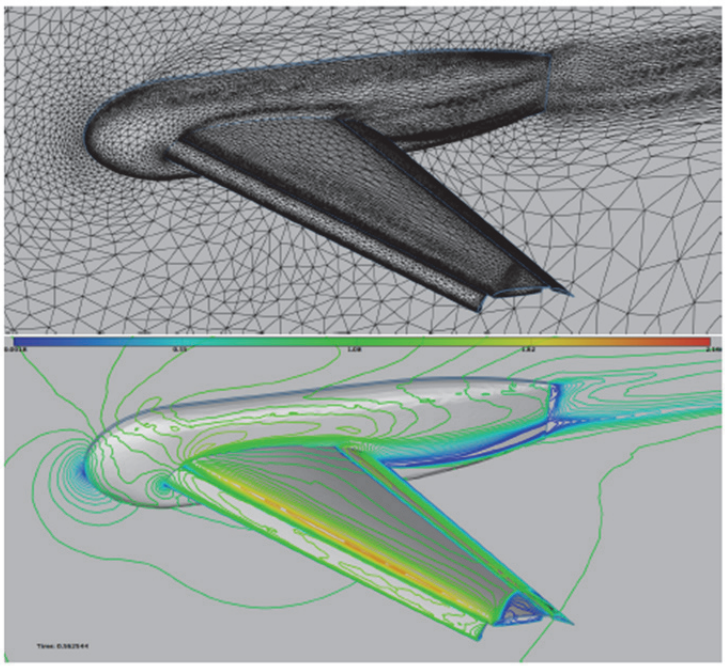

**Figure 6.8.** *Feature-based adaptation for minimizing the $L^1$ norm of the interpolation error on Mach number. Top: View of the skin mesh. There is not much mesh concentration on the body in the wake of wing. Bottom: Velocity on the aircraft skin*

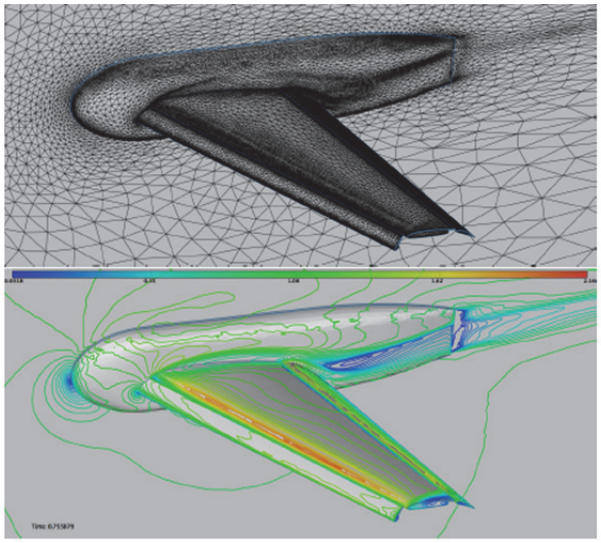

**Figure 6.9.** *Adaptation for minimizing the norm $||W - Wh||_{L^2}$ with the norm-oriented approach. Top: view of the skin mesh. Near-body mesh is finer and shows much more details on the aircraft body. Bottom: Velocity on the aircraft skin.*

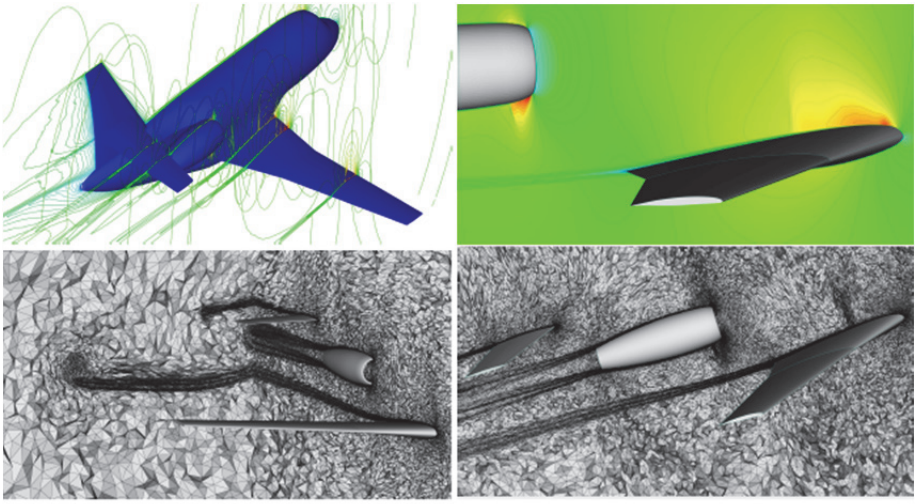

**Figure 6.10.** *Top: Mach solution field. Bottom: final adapted mesh. Shape: courtesy of Dassault Aviation*


**Figure 7.3.** *Initial blast solution (about center of bottom) and location of target surface S*

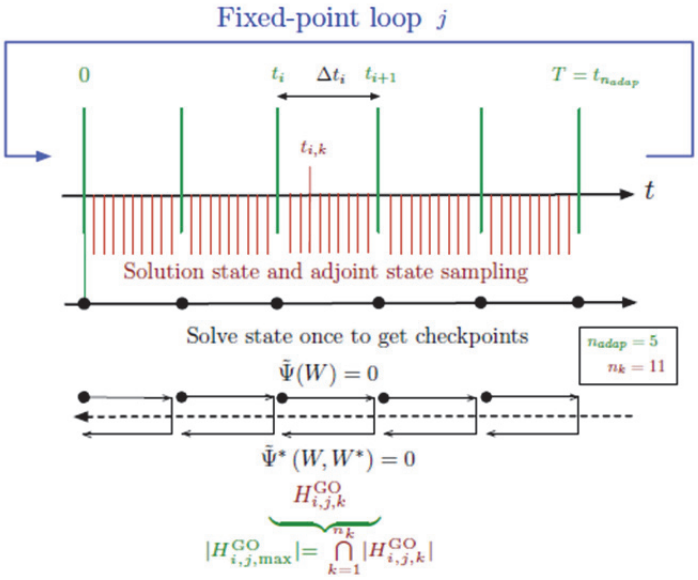


**Figure 7.6.** *Global transient fixed-point algorithm for unsteady goal-oriented anisotropic mesh adaptation*

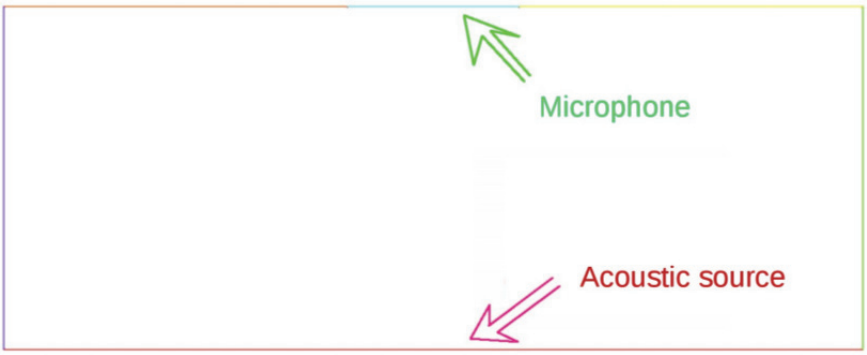


**Figure 7.7.** *Propagation in a box: sketch of geometry. An acoustic source produces sound at the center of the bottom. The microphone integrates the pressure variation on a segment of the top wall*

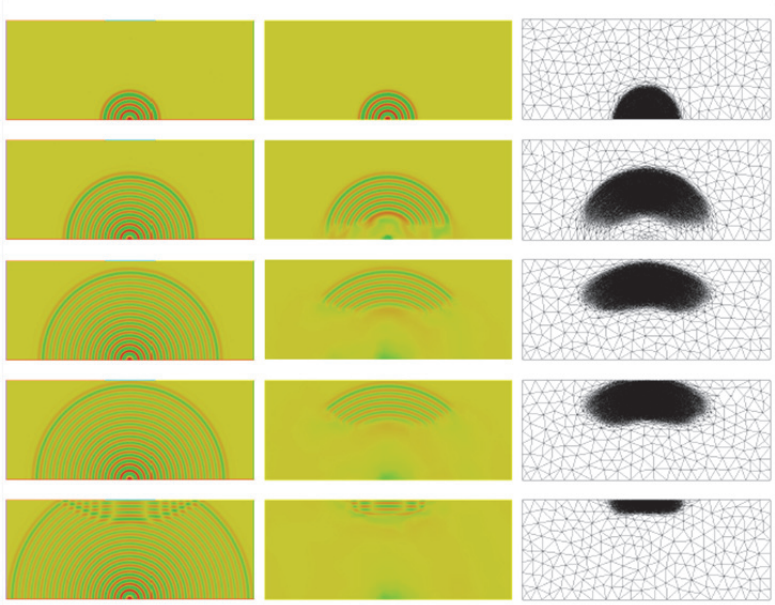

**Figure 7.8.** *Propagation of acoustic waves: density field evolving in time on a uniform mesh (left) and on adapted meshes (middle and right)*

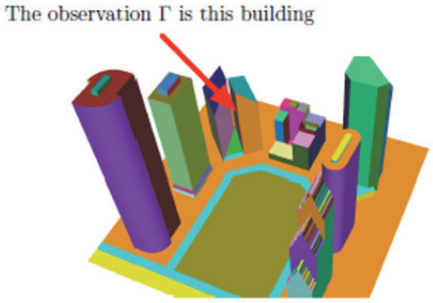


**Figure 7.9.** *3D City test case geometry and location of target surface Γ (surface of the building indicated by the arrow)*

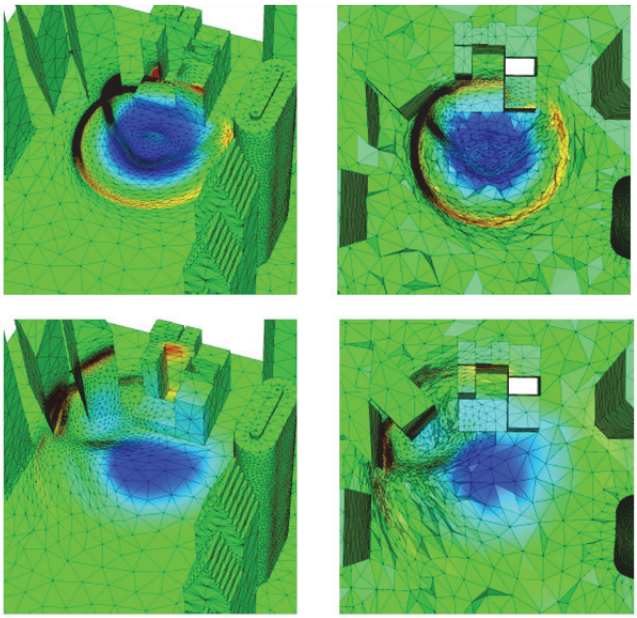

**Figure 7.10.** *3D Blast wave propagation: adjoint-based adapted surface (left) and volume (right) meshes at sub-intervals 10 and 20 and corresponding solution density at a-dimensioned times 5 and 10*

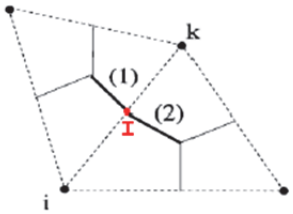


**Figure 8.2.** *Sketch of the interface $\partial C_i \cap \partial C_k$ between cell $C_i$ and cell $C_k$. It is made of two segments (1) and (2) joining mid-edge $I$ and triangles centroid. Flux integration on (1) (respectively, (2)) will rely on two Gauss integration points.*

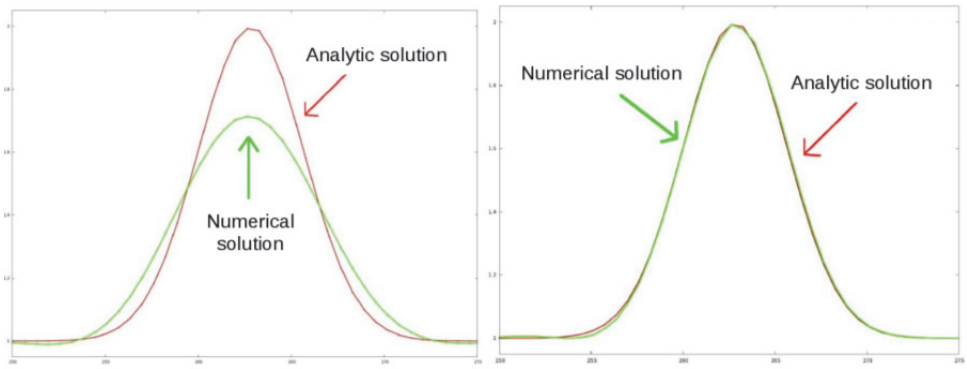


**Figure 8.3.** *Improvement of the CENO scheme for the advection of a 2D Gaussshaped concentration through 400 space intervals. Left: Comparison of the upwind third-order accurate CENO solution with the analytic solution. Right: Comparison of the improved (third-order accurate) CENO scheme with the analytic solution*

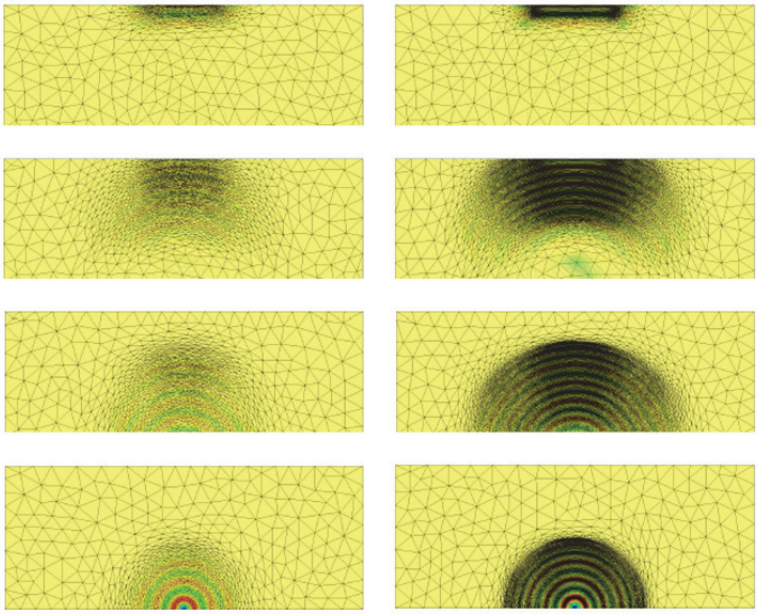

**Figure 8.4.** *Acoustic waves traveling in a box from bottom (5th mesh in time) to top (20th mesh in time) with the coarse option (left, 1,500 vertices in the mean) and the finest option (right, 21,566 vertices in the mean)*

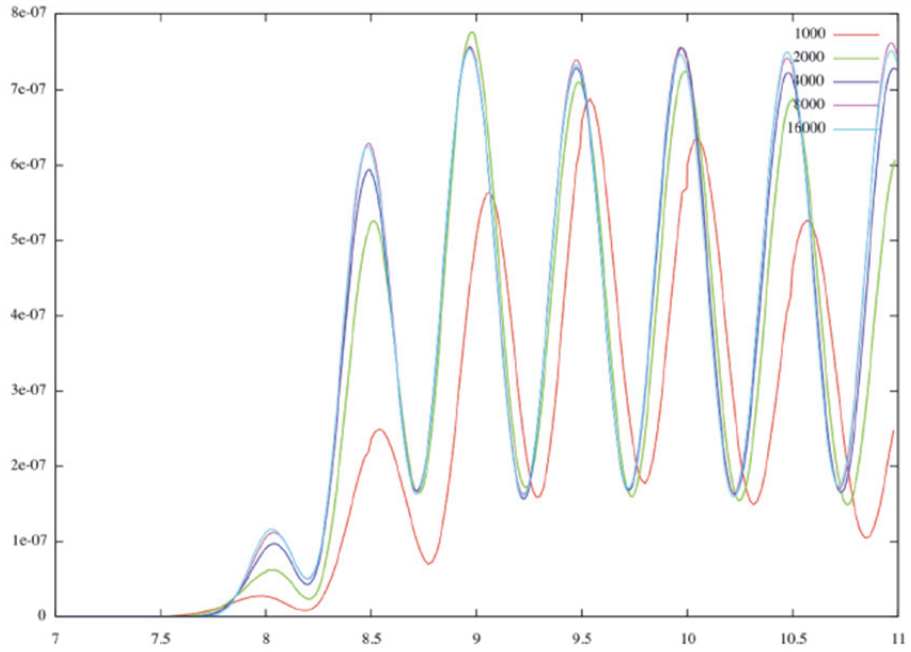


**Figure 8.5.** *Noise propagation in a box: mesh convergence of the spatial integral k(t) (y-axis) as a function of time (x-axis). The lower curve "1000" corresponds to a mean mesh size of 1,500 vertices. The three other curves, almost undistinguishable, correspond to mean mesh sizes of 5,400, 11,000 and 21,000 vertices*